Macromolecules

pubs.acs.org/Macromolecules Article

A New Semicrystalline Polymer from Renewable Source: Poly-1,4-(3-methylene-cyclopentene) as an Example of Three-Dimensional Topotactic Transition Triggered by Temperature

Claudia Napolitano, Veronica Paradiso, Marco Naddeo, David Hermann Lamparelli, Fabia Grisi, Odda Ruiz de Ballesteros, Giuseppe Femina, Carmine Capacchione,* and Finizia Auriemma*

Cite This: *Macromolecules* 2024, 57, 7409−7417 Read Online

ACCESS | Metrics & More | Article Recommendations | Supporting Information

ABSTRACT: In search for biobased alternatives to fossil-based polymers, a synthetic approach is developed that allows the polymerization of a terpene-derived monomer, 3-methylene-cyclopentene (MCP), to poly-1,4-MCP (pMCP) with a high yield and elevated molecular mass. The so-obtained pMCP is regioregular, has an endocyclic double bond/monomer in a fixed *cis* configuration, and is characterized by random enchainment of monomers with the tertiary C atom in *R* and *S* configurations. Yet, it crystallizes from the melt with chains in a nearly extended conformation (average chain periodicity $c \approx 0.96$ nm) in the monoclinic system. Upon heating, the low-temperature crystalline (LTC) form transforms, before melting, in a disordered, high-temperature crystalline form (HTC), characterized by the same extended conformation of the LTC form, and orthorhombic crystals of larger apparent coherence length, through a three-dimensional topotactic transition. This transition entails that close neighboring coherence domains of the LTC form rearrange themselves, forming domains of large size not only along the lattice directions of the unit cell perpendicular to the chain axes but also parallel to the chain axes. This unique temperature-driven LTC → HTC topotactic transition is reversible and, upon cooling, the large HTC domains break, forming smaller domains of the LTC form.

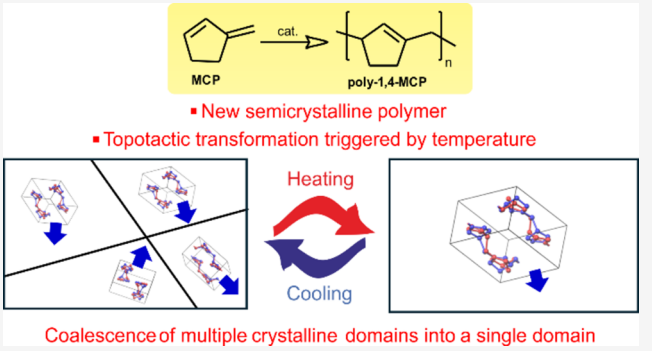

INTRODUCTION

The search for biobased alternatives to polymers based on chemicals arising from fossil resources is an active task of research in both academic and industrial environments not only for the possibility to mitigate the negative effects of using petroleum-based products but also for the possibility of having access to a wider variety of chemical structures due to the higher chemical complexity of the biomass compared to nonrenewable chemicals.[1−4]

In this scenario, much attention has been devoted to monomers coming from sugars and fatty acid derivatives that allow the synthesis of polyesters and polycarbonates.[5−9]

In the realm of natural products, terpenes represent a particularly interesting class of molecules for polymer chemists due to the presence of conjugated double bonds that offer both the opportunity to further functionalization or to directly polymerize these molecules in analogy to 1,3-alkadienes such as butadiene or isoprene.[10−13] As a matter of fact, the stereoregular polymerization of acyclic terpenes has been investigated by using many catalytic systems, giving macromolecules various microstructural features and in some cases physical properties analogous to those of elastomers based on nonrenewable monomers.[14−18] It is worth noting that, with a few exceptions,[17] due to the long alkyl chain of the starting monomers such as myrcene, ocimene, and farnesene, even the highly stereoregular polymers do not show any crystallinity, limiting the possible application of polymers derived from terpenes.

An alternative approach in the polymerization of terpene-derived molecules has been elegantly developed by Hillmyer and co-workers that synthesized the cyclic diene 3-methylene-cyclopentene (MCP) by ring-closing metathesis (RCM) from myrcene and subsequently polymerized the resultant monomer by controlled cationic polymerization to highly regioregular semicrystalline poly-1,4-MCP (pMCP), showing a melting point of 105 °C.[19] More recently, Cui and co-workers also reported the polymerization of MCP promoted by rare-earth precursors, obtaining a highly regioregular pMCP with higher

Received: July 6, 2024
Accepted: July 17, 2024
Published: July 24, 2024

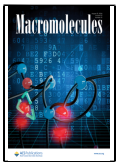

https://doi.org/10.1021/acs.macromol.4c01563
Macromolecules 2024, 57, 7409−7417

melting point (up to 116 °C) compared to the polymer obtained via a carbocationic mechanism.[20]

Here, we describe a different synthetic route to obtain highly regioregular poly-1,4-MCP (pMCP) by using a catalytic system based on the titanium [OSSO]-type complex **1**. The polymer has an endocyclic double bond/monomer in a fixed *cis* configuration and is nonchiral as it is characterized by random enchainment of monomers with the tertiary C atoms of cyclopentene rings in *R* or *S* configuration (Figure 1). The

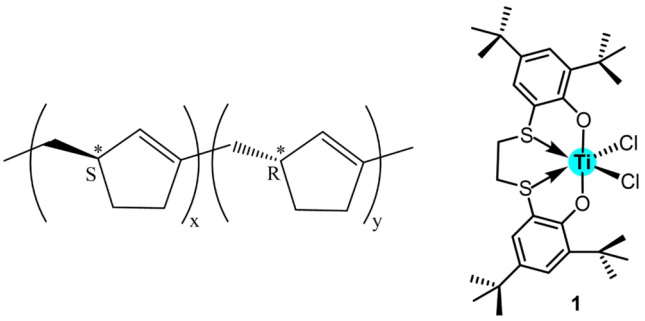

Figure 1. Poly(1,4-MCP) (pMCP) (A) and dichloro{1,4-dithiabutanediyl-2,2′-bis(4,6-di-*tert*-butylphenyl)}titanium (1) (B). The configurations of the asymmetric C atoms of the cyclopentene rings are indicated in panel (A).

structural transitions of the pMCP crystalline form are analyzed as a function of temperature, and limit-ordered and limit-disordered models of the crystal structures are extracted from X-ray diffraction analysis. It is shown that the pMCP crystallizes at room temperature in a monoclinic unit cell, housing large amounts of structural disorder. As the temperature increases, the low-temperature crystalline (LTC) form transforms into a high-temperature crystalline (HTC) form with orthorhombic unit cell parameters, forming crystals with increased coherence length along the three directions of the unit cell parameters through a topotactic three-dimensional mechanism. In view of the large interest in commodity polymers from sustainable resources, the identification of a suitable synthetic approach, polymorphism, and properties of pMCP is the first step toward the industrial development of terpene-based *homo*- and copolymers using monomers derived from biomasses as raw materials.

EXPERIMENTAL SECTION

Details of materials and synthetic approach, of mechanical test experiments, and fiber diffraction analysis are given in the Supporting Information (SI).

Differential scanning calorimetry (DSC) measurements were carried out with a Mettler Toledo DSC-822 apparatus in a flowing N_2 atmosphere at a rate of 10 °C/min.

X-ray powder diffraction (WAXS) profiles were collected as a function of the temperature (from 25 to 150 °C) in reflection geometry using a multipurpose PANalytical Empyrean Diffractometer, by performing $\theta-\theta$ scans (where 2θ is the scattering angle), using Ni filtered Cu Kα radiation (λ = 0.15418 nm). The WAXS apparatus was equipped with a PIXcel^{3D} detector and a nonambient Anton Parr TTK-450 camera. After subtraction of the background contribution to the WAXS intensity, approximated by a straight line spanning the whole sampled 2θ region, the WAXS crystallinity index x_c(WAXS) was evaluated as

$$x_c(\text{WAXS}) = 100\, A_c / A_{tot} \quad (1)$$

where A_c and A_{tot} are the areas of the crystalline phase and the total areas subtending the diffraction profile, respectively. The value of A_c was calculated by subtracting the contribution from the amorphous phase A_a to A_{tot}. The contribution from the amorphous phase was approximated by the WAXS profiles of the samples in the molten state recorded at 150 °C. Due to thermal expansion, the WAXS profile of the melt was translated along the 2θ axis, to shift the maximum from $2\theta \approx 18$ to $\approx 19°$, coincident with the position of the maximum of the amorphous phase at room temperature. The so-calculated value of x_c(WAXS) for the profiles recorded at 25 and 67 °C is around 23%.

The density of the pMCP samples ρ was determined at 25 °C using a hydrostatic balance, weighing small fragments of the sample in air (w_a) and in water (w_w) as

$$\rho = w_a \rho_w / (w_a - w_w) \quad (2)$$

where ρ_w is the density of water at 25 °C (=1 g/cm^3). The so-determined experimental density value corresponds to 1.02 ± 0.05 g/cm^3.

Further details of the characterization methods and structural analyses are given in the SI.

RESULTS AND DISCUSSION

Synthetic Approach. Due to the high versatility of the [OSSO]-type titanium complexes, after their activation with methylalumoxane (MAO), in the stereoselective polymerization of various dienes,[11,21−23] we decided to investigate the polymerization of MCP promoted by complex **1** (Figure 1). Since MAO is well-known to be also a cationic initiator in the polymerization of dienes such as isobutylene, isoprene, and cyclopentadiene,[24,25] we first decided to evaluate the polymerization in the presence of MAO alone (see Table 1, entry 1).

The polymerization proceeds at room temperature very fast with a low yield, producing a polymer with broad dispersity. A similar behavior was observed by using organoborate [Ph_3C][$B(C_6F_5)_4$] with a higher yield. In both cases, the ^{1}H and ^{13}C NMR analyses show the selective formation of pMCP (see the Supporting Information for details), but the melting points are sensibly lower than those reported previously. Notably, using a 5-fold excess of Al^{i}Bu$_3$ as Lewis acid additive leads to narrower dispersity (Table 1, entries 3−5).

Table 1. Cationic Polymerization of 3-Methylene-cyclopentene (MCP)

entry[a]	initiator (I)	AlR_3	MCP/I (mol)	time (min)	yield (%)	M_w[d] (kDa)	M_n[d] (kDa)	$Đ$[d]	T_g[e] (°C)	T_m[e] (°C)
1[b]	MAO		5	5	32	111	24	4.6	3	91
2	[Ph_3C][$B(C_6F_5)_4$]		200	1	99	226	50	4.5	3	91
3	[Ph_3C][$B(C_6F_5)_4$]	Al^{i}Bu$_3$	200	1	99	119	44	2.7	5	96
4[c]	[Ph_3C][$B(C_6F_5)_4$]	Al^{i}Bu$_3$	200	1	99	6.5	2.3	2.8	3	92
5	[Ph_3C][$B(C_6F_5)_4$]	Al^{i}Bu$_3$	800	1	99	138	66	2.1	3	93

[a]Experimental conditions: T = 25 °C, initiator = 9.2 mg ($1.0\cdot10^{-5}$ mol), [AlR_3]/[I] = 5, [MCP] = 0.4 M, toluene. [b]Initiator = 15.0 mg ($2.5\cdot10^{-4}$ mol), [MCP] = 0.1 M. [c][MCP] = 0.1 M. [d]Determined by gel permeation chromatography (GPC). [e]Determined by differential scanning calorimetry (DSC), in the second heating scan (SI).

https://doi.org/10.1021/acs.macromol.4c01563
Macromolecules 2024, 57, 7409−7417

Table 2. Polymerization of MCP Using 1/[Ph_3C][$B(C_6F_5)_4$]/Al^iBu_3 as a Ternary Catalytic System

entry[a]	MCP/I (mol)	T (°C)	time (min)	yield (%)	M_w[d] (kDa)	M_n[d] (kDa)	$Đ$[d]	T_g[e] (°C)	T_m (°C)	ΔH_m[f] (J/g)	T_c[f] (°C)	ΔH_c[f] (J/g)
1	500	25	10	99	214	143	1.5	2/−1.4[f]	65/101	4/15	56/67	3/13
2[b]	80	25	5	99	2.5	1.4	1.8	4	65/101			
3[c]	40	−20	1.5	99	2.3	1.3	1.8	5	65/103			

[a]Experimental conditions: catalyst **1** = 3.1 mg ($1.5\cdot10^{-5}$ mol), [Ti]/[A]/[Al^iBu_3] = 1/1/5, [MCP] = 0.25 M, toluene, [Ph_3C][$B(C_6F_5)_4$] = A. [b][MCP] = 0.1 M. [c][MCP] = 0.03 M. [d]Determined by GPC. [e]Determined by differential scanning calorimetry (DSC) in the second heating scan (SI). [f]From DSC thermograms of Figure 2A.

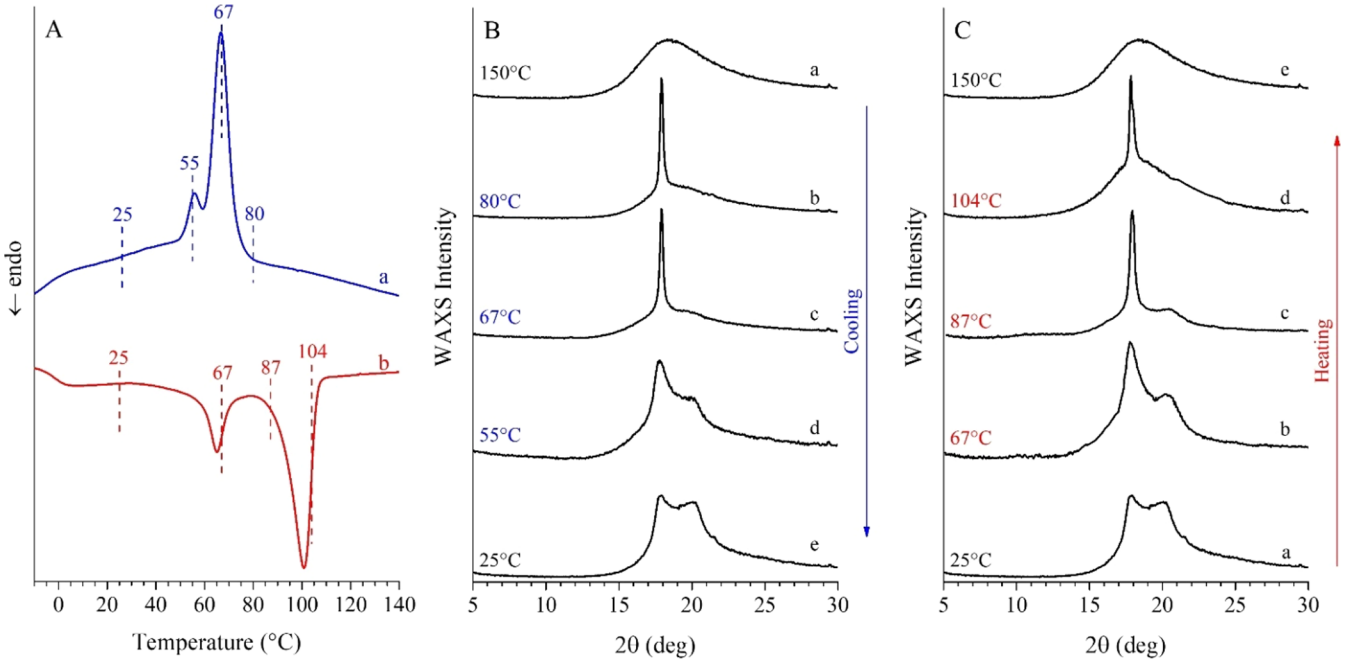

Figure 2. DSC thermograms (A) and X-ray powder diffraction profiles (B, C) of the as-polymerized pMCP sample (entry 1 of Table 2), recorded after melting at 150 °C and 5 min holding the sample at this temperature, in the successive cooling (B) and II heating (C) steps (scanning rate of 10 °C/min). Data in panels (B, C) are collected by cooling and then heating the sample step-by-step from 150 to 25 °C, and from 25 to 150 °C, respectively, while holding the sample at the indicated temperatures during measurements, for a total of about 11 min (2 min isotherm followed by 9 min of measuring time). The selected temperatures for the collection of diffraction data in panels (B, C) are marked in panel (A) (numbers in °C).

Owing these results in hand, we decided to use the ternary system **1**/[Ph_3C][$B(C_6F_5)_4$]/Al^iBu_3 to promote the polymerization of MCP in the presence of the Lewis acidic titanium complex **1**. The results are reported in Table 2.

The polymerization proceeds very fast also in this case with complete conversion of the monomer after a few minutes. The regiopure pMCPs (M_n up to 143 kDa) displayed, in the second heating scan, double melting temperatures around 63 and 101 °C and glass transition temperatures (T_g) around 2−5 °C.

The high stereoselectivity and activity of catalytic system **1**/[Ph_3C][$B(C_6F_5)_4$]/Al^iBu_3 allowed us to obtain a large amount of the high molecular mass sample, entry 1 of Table 2, for further characterization studies.

Structural and Thermal Characterization. DSC thermograms of the as-polymerized (pristine) pMCP sample (entry 1 of Table 2) were recorded after a first heating step until a maximum temperature T_{max} of 150 °C was reached (data not shown), followed by a 5 min isotherm at T_{max}. The thermograms collected in the successive cooling and heating scans are reported in Figure 2A.

The sample shows a crystallization peak at ≈67 °C followed by a small peak at 56 °C (curve a in Figure 2A). In the successive heating scan, two endothermic peaks are present at ≈65 and 101 °C (enthalpy values of ≈4 and 15 J/g, respectively), while the glass transition temperature shifts to −1.4 °C. Compared to the DSC thermogram of Figure S24, the decrease of T_g may be ascribed to some relaxation of the melt during the isotherm at T_{max}.

The powder X-ray diffraction profiles (Figure 2B) recorded during cooling reveal at 80 and 67 °C the presence of a narrow reflection at $2\theta \approx 18°$ (interplanar spacing $d \approx 0.49$ nm, curves *b*,*c*), overlaying an amorphous halo (Table S1) flanked by a broad reflection at $2\theta \approx 20°$ of low intensity. At temperatures lower than 67 °C, the reflection at $2\theta \approx 18°$ gradually broadens and the reflection at $2\theta \approx 20°$ ($d \approx 0.44$ nm) emerges, the relative intensity of which increases as the temperature decreases (curves *d*−*f* and Table S1). These changes are reversible. During the successive heating (Figure 2C), the relative intensity of the reflection at $2\theta \approx 18°$ tends to increase, and that of the reflection at $2\theta \approx 20°$ tends to decrease. At temperatures greater than 67 °C, the reflection at $2\theta \approx 20°$ disappears almost completely, and the diffraction profile becomes dominated by the presence of the narrow reflection at $2\theta \approx 18°$.

The data in Figure 2 indicate that the pMCP sample shows polymorphic behavior. It crystallizes from the melt in a high-

https://doi.org/10.1021/acs.macromol.4c01563
Macromolecules 2024, 57, 7409−7417

temperature crystalline form (HTC), with chains organized in domains characterized by large coherence lengths. As the temperature decreases, the HTC domains break, and the HTC form transforms in a low-temperature crystalline form (LTC). Upon heating, the LTC form transforms back to the HTC form before melting. The crystallinity indexes evaluated from the X-ray powder diffraction profiles recorded at 25 and 67 °C during cooling are similar, around 23%.

The fiber diffraction pattern of pMCP crystallized from the melt in the LTC form and then stretched at deformation close to rupture (350%; see Figure S27) is shown in Figure S28. It reveals the presence of two diffraction peaks at $d \approx 0.44$ and 0.48 nm on the equator, along with a diffraction peak on the first layer line at $d \approx 0.44$ nm (see Table S2). A meridional reflection is also present on the second layer line at $d \approx 0.48$ nm, the position of which cannot be precisely determined.

These results indicate that the reflection at $2\theta \approx 20°$ ($d \approx 0.44$ nm) observed in the X-ray powder diffraction profile of the LTC form (curve e of Figure 2B), upon stretching, becomes polarized on the equator and the first layer line, whereas the diffraction peak at $2\theta \approx 18°$ ($d \approx 0.48$ nm) becomes polarized on the equator and on the second layer line. From the value of the cylindrical coordinate ζ (= n/c, with n the layer line number) of the reflections on the first and second layer lines, an average chain periodicity c close to 0.96 nm may be roughly estimated. The diffraction data of the LTC and HTC forms could be tentatively indexed with an orthorhombic unit cell with parameters $a = 0.90$, $b = 0.59$, and $c = 0.96$ nm. Assuming the presence of four monomeric units/cell, the calculated value of density ρ corresponds to 1.04 g/cm^3, in close agreement with the experimental density value of 1.02 ± 0.05 g/cm^3. The Miller indices of the observed reflections in the powder (Figure 2B) and fiber diffraction patterns (Figure S28) are reported in Tables S1 and S2. The observed values of 2θ and d of the diffraction peaks are in good agreement with the calculated values.

Conformational Analysis. Minimum energy conformations for the pMCP chains suitable for the crystalline state were found by performing calculations of the potential energy surface (PES) on the model dimers of Figure S29. The internal energy was scanned as a function of the internal torsion angles θ_1 (C_1-C_2-↑-C_3-C_4) and θ_2 (C_2-C_3-↑-C_4-C_5), defined in Figure 1A (see also Figure S29) while minimizing the energy with respect to all remaining variables. Minimum energy conformations correspond to values of θ_1 and θ_2 in the states $G^{\pm}$ $G^{\pm}$ (= ±60 ±30°), TT (= 180 ± 30°), $G^{\pm}$ $G^{\mp}$ (= ∓60 ± 30°), and $TG^{\pm}$ and $G^{\pm}T$, regardless of the chirality of the asymmetric carbon atom (C_2*, Figure S29). The minima have similar energy, with differences lower than 1 kcal/mol.

Possible conformational models of pMCP chains suitable for the crystalline state of low internal energy were built up by setting the conformation of the monomeric units in the minima of Figure S29. They are shown in Figure 3.

The models of Figure 3A,A′,B,B′ correspond to configurationally ordered isotactic chains with isochiral asymmetric carbon atoms that are all in the *R* (Figure 3A,A′, *R*-pMCP) and *S* (Figure 3B,B′, *S*-pMCP) configurations (i.e., all *m* diads). The isotactic configuration of the *R*- and *S*-pMCP chains is compatible with the line repetition group $s(2/1)$,[26] which corresponds to the identical repetition every two consecutive monomeric units, and a succession of internal rotation angles of kind $(\theta_1,\theta_2)_n$. Models with chain periodicity equal to ≈0.96 nm were then built up, by setting $(\theta_1,\theta_2)_n$ equal to $(77,89°)_n$ for the *R*-pMCP and to $(-77,-89°)_n$ for the *S*-pMCP chains (Figure 3A,B), close to minima 5 and 1 of Figure S29A,B, respectively.

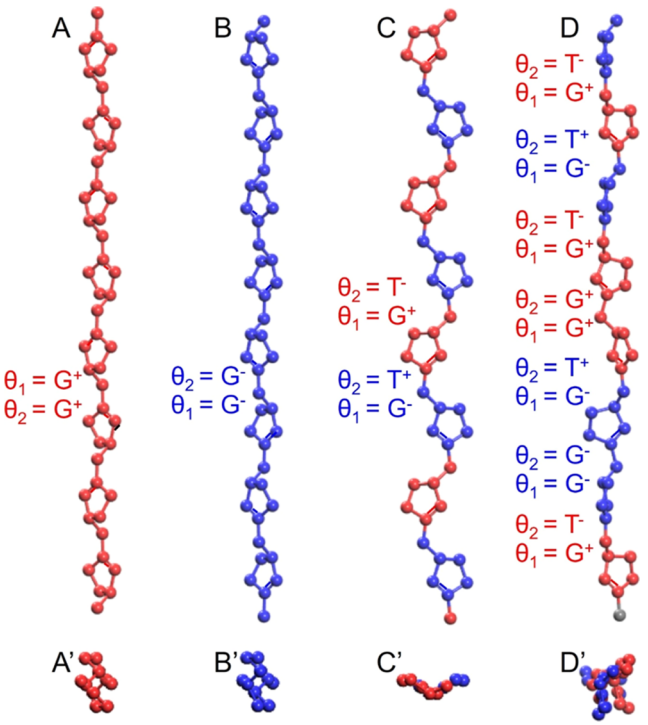

Figure 3. Possible conformational models of low internal energy suitable for pMCP chains in the crystalline state in projections parallel (A−D) and perpendicular (A′−D′) to the chain axes. The values of the internal torsion angles θ_1 and θ_2 are indicated. The chirality of the tertiary C atom of the cyclopentene rings is outlined in red for the *R* configuration and in blue for the *S* configuration. The models (A, B) correspond to isotactic *R*- and *S*-pMCP. The models (C, C′) correspond to syndiotactic pMCP. The models (D, D′) correspond to atactic pMCP. The chains have a directional property, depending on whether the five-carbon rings point with the double bond upward (up) or downward (down), along the chain axis.

The model of Figure 3C,C′ corresponds to a configurationally ordered syndiotactic chain with asymmetric carbon atoms alternating along the chain in the *R* and *S* configurations (i.e., all *r* diads). The syndiotactic configuration of pMCP chains is compatible with the line repetition group **t***c*,[26] which corresponds to the identical repetition every two consecutive monomeric units, and a succession of internal rotation angles of kind $(\theta_1,\theta_2,-\theta_1,-\theta_2)_n$. Models with chain periodicity equal to ≈0.96 nm were built up, by setting $(\theta_1,\theta_2,-\theta_1,-\theta_2)_n$ equal to $(72,-176,-72,+176°)_n$, close to minima 4 and 3 of Figure S29A,B, respectively.

Finally, the model of Figure 3D,D′ corresponds to a configurationally disordered chain with asymmetric carbon atoms randomly following one another, with equal probability, in the *R* and/or *S* configurations (i.e., random succession of *m* and *r* diads). For atactic pMCP, straight chains of low internal energy, with average chain periodicity close to the halved experimental value of ≈0.48 nm, were easily built up, by setting (θ_1,θ_2) within each diad equal to (G^+,G^+) or (G^-,G^-), for *m* diads consisting of consecutive monomeric units both in *R* or *S* configuration, respectively, (G^+,T^-) or (G^-,T^+) for *r* diads consisting of consecutive monomeric units in *R*,*S* or *S*,*R* configuration, respectively.

https://doi.org/10.1021/acs.macromol.4c01563
Macromolecules 2024, 57, 7409−7417

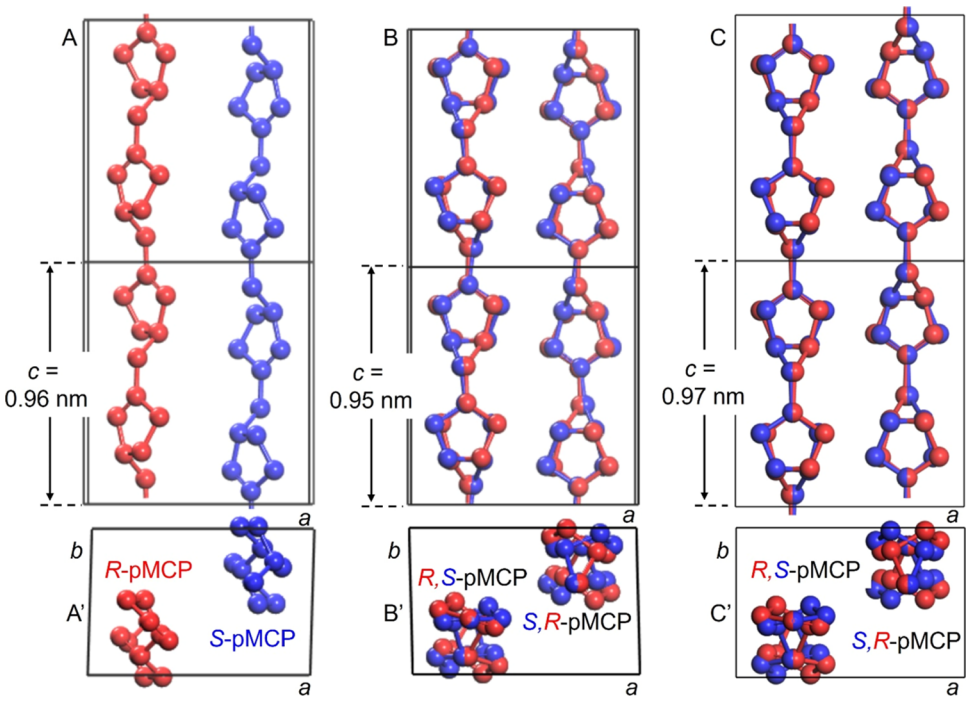

Figure 4. Limit-ordered (A, A′) and limit-disordered (B, B′; C, C′) models of the crystal structure of pMCP in the LTC (A, A′; B, B′) and HTC (C, C′) forms according to the space group symmetry $P2_1/n$ (*c* unique axis) (A, A′; B, B′) and *Pmcn* (C, C′). Configurational disorder in panels (B, B′) and (C, C′) is modeled by assuming that each monomeric unit in the *R* or *S* configuration may be followed along the chain, with the same probability, by a monomeric unit either having the same configuration or opposite configuration, giving rise to a random succession of *m* and *r* diads. The unit cell parameters are $a = 0.892 \pm 0.001$, $b = 0.5879 \pm 0.0005$, $c = 0.96$ (not refined) nm and $\gamma = 88.33 \pm 0.09°$ in panels (A, A′); $a = 0.9141 \pm 0.0008$, $b = 0.5884 \pm 0.0002$, $c = 0.9537 \pm 0.0008$ nm, and $\gamma = 91.47 \pm 0.03°$ in panels (B, B′); and $a = 0.9057 \pm 0.0009$, $b = 0.5913 \pm 0.0003$, $c = 0.9708 \pm 0.0006$ nm in panels (C, C′).

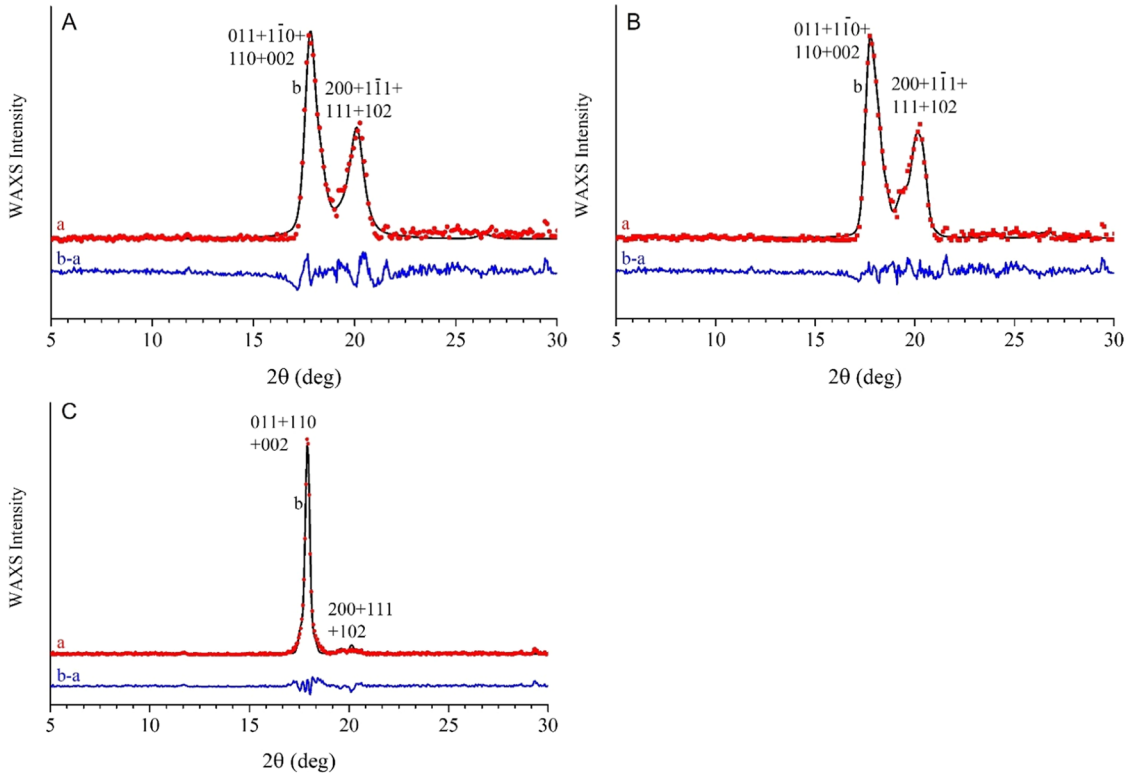

Figure 5. Comparison between the observed (curve *a*) and the Rietveld refined (curve *b*) powder diffraction profiles of pMCP in the LTC (A, B) and HTC (C) forms. Curves "*b*−*a*" are the difference profiles. The Miller indices of the reflections are indicated. The experimental profile a in panels (A, B) corresponds to the WAXS profile e of Figure 2B, and the experimental profile a in panel (C) corresponds to the WAXS profile c of Figure 2B. Calculations in panels (A−C) are relative to the structural models (A−A′), (B−B′), and (C−C′) of Figure 4, respectively.

https://doi.org/10.1021/acs.macromol.4c01563
Macromolecules 2024, 57, 7409−7417

From Figure 3, it is apparent that the pMCP chains have a directional property, depending on whether the five-carbon rings point with the double bond upward (up) or downward (down), along the chain axis. The model chains of Figure 3B−D are down, whereas the model chain of Figure 3A is up. Pairs of isochiral chains both up (down) are said to be isoclined. Pairs of isochiral chains of which one chain is up (down) and the other is down (up) are said to be anticlined.[26]

It is worth noting that the presence of the strong 111 reflection on the first layer (with a nonnegligible intensity; Table S2 and Figure S28) suggests that suitable models of the chain conformation of pMCP for the crystalline state in the LTC form should incorporate two monomeric units/identity period, such as it occurs for the isotactic and/or syndiotactic models of Figure 3A−C,A′−C′. Atactic models including random succession of *r* and *m* diads, such as the model of Figure 3D,D′, instead, are less suitable because the average periodicity would be halved. In the working hypothesis that the chain conformation in the LTC and HTC forms were similar, structural models for the LTC and HTC forms considered in the next section are built up using chains in isotactic and/or syndiotactic (see also the SI) configurations, modeling the configurational disorder in a statistical manner.

Structural Analysis. Possible structural models for the LTC and HTC forms of pMCP are shown in Figure 4, whereas the experimental powder X-ray diffraction profiles are compared with the calculated profiles in Figure 5. For the sake of simplicity, the X-ray diffraction profiles of pMCP recorded at 25 and 67 °C in the cooling steps (curves *e* and *c* of Figure 2B, respectively) have been considered for X-ray modeling of the LTC and HTC forms, respectively. The packing models were refined by performing a full profile analysis of the experimental powder X-ray diffraction profiles with the Rietveld method while introducing constraints at the unit cell boundaries related to the bond distances and valence angles.

As an example, the limit-ordered model of Figure 4A,A′ corresponds to isotactic pMCP chains packed in a monoclinic unit cell according to the space group symmetry $P2_1/n$ (*c* unique axis), with parameters $a = 0.892 \pm 0.001$, $b = 0.5879 \pm 0.0005$, $c = 0.96$ nm, and $\gamma = 88.33 \pm 0.09$. It corresponds to four monomeric units/cell, for a density of 1.0591 g/cm^3, in good agreement with the experimental density value of 1.02 ± 0.05 g/cm^3. The model may be described in terms of *bc* rows of isochiral, isoclined *R*- or *S*-pMCP chains alternating along the *a*-axis with *bc* rows of chains of opposite chirality, *S*- or *R*-pMCP, respectively, which are anticlined with respect to the chains in adjacent rows. In the model, the **s**(2/1) line symmetry of the chain is maintained, and the asymmetric unit corresponds to a single monomeric unit, with fractional coordinates reported in Table S4. The closest distances occur between the H atoms facing *bc* row interfaces and are all greater than 0.215 nm.

In the structural model, the degrees of freedom are the rotation around the chain axis and the translation of the chains parallel to the chain axes (Table S4). In the Rietveld analysis, these variables were refined. The Rietveld refined X-ray powder diffraction profile calculated for the model structure of Figure 4A,A′ is compared with the experimental profile of the LTC form of pMCP in Figure 5A (profile (e) of Figure 2B). It is apparent that the model of Figure 4A,A′ reproduces to a good approximation the diffraction data. The Rietveld reliability factor calculated on the basis of the Rietveld analysis R(Riet) is 13%. The observed structure factors F_o are compared with the calculated ones F_c in Table S5. The reliability factor R evaluated for the sole observed reflections is 4%. Additional reflections are also calculated at $2\theta \approx 22$ and 26° but are hardly observed since their intensity is too low to be confidently measured. The coherence domains of the LTC form have small sizes along *a*- and *c*-axes, with apparent values L_a and L_c of ≈7 nm and greater coherence length along the *b*-axis, with an apparent value L_b of ≈19 nm (see Table S6). This corresponds to arrays of about 7 × 30 × 7 adjacent unit cells, including chains of prevalent isotactic configuration.

A limit-disordered model for the LTC form accounting for the configurational disorder of pMCP chains was also considered. It is shown in Figure 4B,B′. In this model, configurational disorder was modeled by assuming that each monomeric unit in the *R* or *S* configuration may be followed along the chain, with the same probability, by a monomeric unit having either the same configuration or opposite configuration, giving rise to a random succession of *m* and *r* diads. The chains are packed in a monoclinic unit cell according to the space group symmetry $P2_1/n$ (*c* unique axis), with parameters $a = 0.9141 \pm 0.0008$, $b = 0.5884 \pm 0.0002$, $c = 0.9537 \pm 0.0008$ nm, and $\gamma = 91.47 \pm 0.03$°. As before, it corresponds to four monomeric units/cell, for a density of 1.02338 g/cm^3, in good agreement with the experimental density value of 1.02 ± 0.05 g/cm^3. The model may be described in terms of *bc* rows of atactic, isoclined pMCP chains alternating along the *a*-axis with *bc* rows of atactic chains that are anticlined with respect to the chains in adjacent rows. In the model, the asymmetric unit corresponds to two independent monomeric units of opposite chirality located around the special position 1/4, 1/4, *z* of the 2_1 crystallographic axis (occupancy factor = 0.5). The fractional coordinates are reported in Table S8. The closest distances occur between the H atoms facing at *bc* row interfaces and are all greater than 0.2 nm.

The Rietveld refined X-ray powder diffraction profile calculated for the model structure of Figure 4B,B′ is compared with the experimental profile of the LTC form of pMCP in Figure 5B (profile e of Figure 2B). Refinement was carried out with respect to the rotation around the chain axis and the translation of the chains parallel to the chain axes (Table S8). It is apparent that the model of Figure 4B,B′ reproduces to a good approximation the diffraction data. The Rietveld reliability factor calculated on the basis of the Rietveld analysis R(Riet) is 9.55%. The observed structure factors F_o are compared with the calculated ones F_c in Table S9. The reliability factor R calculated for the sole observed reflections is 3%. Also in this case, additional reflections are calculated at $2\theta \approx 24$ and 26° but are not observed. The apparent values of the coherence length of LTC domains along the *a*-, *b*-, and *c*-axes L_a, L_b, and L_c are ≈11, 19, and 26, respectively (Table S10), and correspond to an array of ≈12 × 32 × 27 unit cells along *a*, *b*, and *c*, respectively.

Although the agreement between the experimental and calculated X-ray powder diffraction data can be further improved by introducing additional statistical disorder in the packing of the chains in the unit cell, such as up/down disorder, the limit-disordered model of Figure 4B,B′ may be considered a good description of the crystal structure of the LTC form of pMCP.

As for the HTC form of pMCP, several structural models were built up in the working hypothesis that the chain

https://doi.org/10.1021/acs.macromol.4c01563
Macromolecules 2024, 57, 7409−7417

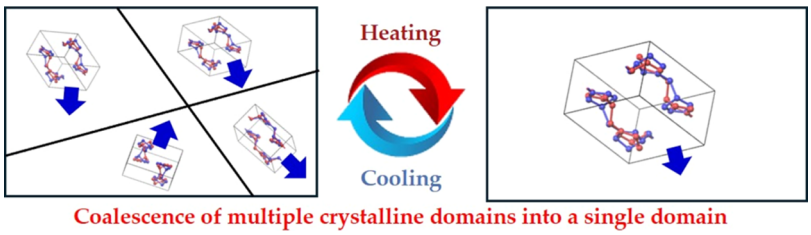

Figure 6. Scheme illustrating the reversible topotactic transformation of the LTC form (left) into the HTC form (right) occurring by increase of the temperature and of the HTC form into the LTC form occurring upon cooling. The relative orientation of the unit cells in the small coherence domains of the LTC form is random. Upon heating, the relative orientation of the chains in close neighboring domains of the LTC form rearranges itself to give rise to large domains of the HTC form. This transition occurs not only in the direction perpendicular to the chain axes but also along the *c*-axes.

periodicity of the LTC form is preserved. The presence of a faint reflection at $2\theta \approx 20°$ ($d \approx 0.44$ nm), reminiscent of the strong reflection at the same 2θ of the LTC form, rules out a pseudohexagonal packing of the chains, since the ratio between the spacings of the reflections at $2\theta \approx 18$ and 20° (i.e., ≈0.496/0.44) is significantly different from $3^{1/2}$. This suggests that the pMCP chains are arranged in an orthorhombic unit cell.

A tentative structural model for the HTC form of pMCP that includes chains in syndiotactic configuration is shown in Figure S30. It corresponds to chains packed in an orthorhombic unit cell, according to the symmetry of space group $Pca2_1$ and parameters $a = 1.0065 \pm 0.0007$, $b = 0.5686 \pm 0.0001$, and $c = 0.9707 \pm 0.0007$ nm. The asymmetric unit corresponds to a single monomeric unit placed around the special position (1/4a) of the glide plane *c* perpendicular to *a*. In this way, the **t***c* line symmetry of the chains is maintained, and only one degree of freedom is left, corresponding to the translation of the chains along the *b*-axis.

Even though the Rietveld refined X-ray powder diffraction profile reproduces with a good approximation the experimental profile (Figure S31) by placing the center of mass of the chains at 0.25*b* or 0.75*b*, with good contact distances between nonbonded atoms, and the Rietveld reliability factor *R*(Riet) equal to 5.93%, the calculated density $\rho = 0.9581$ g/cm^3 is too low compared with the experimental density value of 1.02 ± 0.05 g/cm^3 (see the SI). Moreover, the reliability factor *R* calculated for the sole observed reflections is 20%.

Additional symmetries of the space groups for pMCP in the HTC and/or LTC forms, with chains in syndiotactic configuration, were also attempted, while reducing to a minimum the degree of freedom of the structural parameters, as for instance utilizing the space group symmetry $Pc2_1n$ (data not shown). However, in all cases, the agreement was not satisfactory. This indicates that a prevailing syndiotactic configuration for the pMCP chains in the HTC and LTC forms is not suitable.

A better agreement was instead obtained for the limited disordered model structure of atactic pMCP chains packed in an orthorhombic unit cell, according to the statistical space group symmetry *Pmcn*. The structural model is shown in Figure 4C,C′. This model is well-suited for the description of the chain packing of pMCP in the HTC form. Similar to the limit-disordered model structure of pMCP in the LTC form of Figure 4B,B′, also for the model of Figure 4C,C′, configurational disorder was modeled by assuming that each monomeric unit in the *R* or *S* configuration may be followed along the chain, with equal probability, by a monomeric unit having either the same configuration or opposite configuration, giving rise to a random succession of *m* and *r* diads. The unit cell parameters are $a = 0.9057 \pm 0.0009$, $b = 0.5913 \pm 0.0003$, and $c = 0.9708 \pm 0.0006$ nm (Table S11). The asymmetric unit corresponds to a single monomeric unit, with an occupancy factor of 1/2, located in a position close to the mirror plane symmetry *m* at 1/4a. The fractional coordinates of the asymmetric unit are reported in Table S12. The number of monomeric units/cells is four, corresponding to a density of 1.02338 g/cm^3, in good agreement with the experimental density value of 1.02 ± 0.05 g/cm^3.

Similar to the model of Figure 4B,B′, *bc* rows of atactic, isoclined pMCP chains alternate along the *a*-axis with *bc* rows of atactic chains, which are anticlined with respect to the chains in adjacent rows. The closest (optimized) distances occur between the H atoms facing *bc* row interfaces and are greater than 0.2 nm.

The Rietveld refined powder X-ray diffraction profile calculated for the model structure of Figure 4C,C′ is compared with the experimental profile of the HTC form of pMCP in Figure 5C (profile c of Figure 2B). It is apparent that the model of Figure 4C,C′ reproduces to a good approximation the diffraction data. The Rietveld reliability factor calculated on the basis of Rietveld analysis, *R*(Riet), is 7.81%. The observed structure factors F_o are compared with the calculated ones F_c in Table S13. The reliability factor calculated for all of the reflections is 5%. It is worth noting that the apparent values of the coherence length of HTC domains along *a*-, *b*-, and c-axes L_a, L_b, and L_c are significantly greater than those of the LTC form, and equal to ≈27, 43, and 44 nm, respectively (Table S14), corresponding to arrays of ≈30 × 72 × 45 unit cells along *a*, *b*, and *c*, respectively.

Therefore, the LTC → HTC phase transition induced at high temperatures entails an increase of the coherence length of the crystalline domains not only along *a* and *b* but also along *c*. This transition involves small rearrangements of the chain conformation and in the relative position and orientation of the chains within the unit cell but big changes in the relative orientation of the chains belonging to close neighboring coherence domains, as in a topotactic transition (Figure 6). These changes occur not only in the directions perpendicular to the chain axes but also parallel to the chain axes.

We argue that as the temperature increases above a threshold, atactic stems of pMCP crystallizing in neighboring domains along *c* change their relative orientation and position until they reach a full register in the average atomic positions. This transition is reversible. Upon cooling, the large domains of the HTC form break, forming smaller domains of the LTC form.

https://doi.org/10.1021/acs.macromol.4c01563
Macromolecules 2024, 57, 7409−7417

Topotactic transitions are quite common for metal oxides.[27−29] A topotactic mechanism has been also proposed for the transformation of graphite to diamond.[30] However, topotactic transitions have rarely been observed for polymers. As an example, it has been shown that ethylene-tetrafluoroethylene (ETFE) copolymers, containing 50−70 mol % of tetrafluoroethylene, crystallize at low temperatures in an orthorhombic form, which transforms at high temperatures in a pseudohexagonal mesomorphic form, through a topotactic mechanism.[31,32] This transition involves a neat increase of the coherence length of the pseudohexagonal domains in the lattice directions perpendicular to the chain axes, as indicated by the strong narrowing of the equatorial diffraction peak in the corresponding X-ray powder diffraction profiles. For pMCP, the topotactic transition occurs along all three lattice directions, and the increase of coherence length along the *b*-axis is more pronounced than that occurring along the *a*- and *c*-axes. It represents a rare case of a three-dimensional (3D) topotactic transition in polymers.

CONCLUSIONS

In the urge for the increase of knowledge about synthetic strategies, structure, and properties of polymers from renewable resources, the present study proposes a new process to obtain high yield, highly regioregular pMCP, from a myrcene-derived monomer, 3-methylene-cyclopentene, by using a catalyst based on titanium, an Earth-crust abundant metal. It is shown that pMCP is crystalline, even if it is atactic. It melts at 101 °C, shows good mechanical properties, and experiences a reversible crystal−crystal phase transition triggered by the temperature.

This transition involves a neat increase of the coherence length of the crystalline domains of the polymorph stable at low-temperature LTC, not only along the lattice directions perpendicular to the chain axes but also parallel to the chain axes. A 3D topotactic mechanism is proposed to explain the temperature-induced, reversible phase transition between the LTC and HTC forms of pMCP.

The unique LTC and HTC structures of pMCP represent an example of solid mesophases in polymers characterized by the parallel arrangement of chains with long-range order of an average motif along all three lattice directions of the unit cell, despite configurational disorder.[32]

ASSOCIATED CONTENT

Supporting Information

The Supporting Information is available free of charge at https://pubs.acs.org/doi/10.1021/acs.macromol.4c01563.

General remarks; reagents and complexes; typical MCP polymerization procedure; NMR-selected spectra; GPC selected analysis; DSC-selected analysis; WAXS results; stress−strain curve; X-ray fiber diffraction analysis; conformational analysis; crystal structure analysis; optimized structural and nonstructural parameters in Rietveld analysis; values of structural and nonstructural parameters optimized in the Rietveld analysis for the limit-ordered and limit-disordered model structure of pMCP in the LTC and HTC forms of Figure 4; and limit-ordered model structure of pMCP in the HTC form, with space group symmetry *Pca*21 and calculated diffraction profile; the CIF files of the structural models of Figures 4 and S30 are also provided (PDF)

AUTHOR INFORMATION

Corresponding Authors

Carmine Capacchione − *Department of Chemistry and Biology 'Adolfo Zambelli, University of Salerno, 84084 Fisciano, Italy;* orcid.org/0000-0001-7254-8620; Email: ccapacchione@unisa.it

Finizia Auriemma − *Department of Chemical Science, University of Napoli Federico II, Complesso Monte S. Angelo, 80126 Napoli, Italy;* orcid.org/0000-0003-4604-2057; Email: finizia.auriemma@unina.it

Authors

Claudia Napolitano − *Department of Chemical Science, University of Napoli Federico II, Complesso Monte S. Angelo, 80126 Napoli, Italy*

Veronica Paradiso − *Department of Chemistry and Biology 'Adolfo Zambelli, University of Salerno, 84084 Fisciano, Italy*

Marco Naddeo − *Department of Chemistry and Biology 'Adolfo Zambelli, University of Salerno, 84084 Fisciano, Italy*

David Hermann Lamparelli − *Department of Chemistry and Biology 'Adolfo Zambelli, University of Salerno, 84084 Fisciano, Italy*

Fabia Grisi − *Department of Chemistry and Biology 'Adolfo Zambelli, University of Salerno, 84084 Fisciano, Italy;* orcid.org/0000-0003-3904-9541

Odda Ruiz de Ballesteros − *Department of Chemical Science, University of Napoli Federico II, Complesso Monte S. Angelo, 80126 Napoli, Italy;* orcid.org/0000-0003-4940-421X

Giuseppe Femina − *Department of Chemical Science, University of Napoli Federico II, Complesso Monte S. Angelo, 80126 Napoli, Italy*

Complete contact information is available at: https://pubs.acs.org/10.1021/acs.macromol.4c01563

Author Contributions

The manuscript was written through contributions of all authors. All authors have given approval to the final version of the manuscript.

Notes

The authors declare no competing financial interest.

ACKNOWLEDGMENTS

We acknowledge financial support under the National Recovery and Resilience Plan (NRRP), Mission 4, Component 2, Investment 1.1, Call for tender No. 1409 published on 14.9.2022 by the Italian Ministry of University and Research (MUR), funded by the European Union − NextGenerationEU−Project Title: Sustainable elastomers from natural products for a safer environment (Selene) − CUP D53D23016990001 − Grant Assignment Decree No. 1384 adopted on 01/09/2023 by the Italian Ministry of Ministry of University and Research (MUR). Dr. Patrizia Iannece, Dr. Patrizia Oliva, Dr. Mariagrazia Napoli, and Dr. Ivano Immediata, from Università degli Studi di Salerno, are deeply acknowledged for technical assistance.

REFERENCES

(1) Zhu, Y.; Romain, C.; Williams, C. K. Sustainable Polymers from Renewable Resources. *Nature* **2016**, *540* (7633), 354−362.

(2) Mecking, S. Nature or Petrochemistry?—Biologically Degradable Materials. *Angew. Chem. Int. Ed.* **2004**, *43* (9), 1078−1085.

(3) Gandini, A. Polymers from Renewable Resources: A Challenge for the Future of Macromolecular Materials. *Macromolecules* **2008**, *41* (24), 9491−9504.
(4) Yao, K.; Tang, C. Controlled Polymerization of Next-Generation Renewable Monomers and Beyond. *Macromolecules* **2013**, *46* (5), 1689−1712.
(5) Manker, L. P.; Dick, G. R.; Demongeot, A.; Hedou, M. A.; Rayroud, C.; Rambert, T.; Jones, M. J.; Sulaeva, I.; Vieli, M.; Leterrier, Y.; Potthast, A.; Maréchal, F.; Michaud, V.; Klok, H.-A.; Luterbacher, J. S. Sustainable Polyesters via Direct Functionalization of Lignocellulosic Sugars. *Nat. Chem.* **2022**, *14* (9), 976−984.
(6) Galbis, J. A.; de Gracia García-Martín, M.; de Paz, M. V.; Galbis, E. Synthetic Polymers from Sugar-Based Monomers. *Chem. Rev.* **2016**, *116* (3), 1600−1636.
(7) Brandolese, A.; Lamparelli, D. H.; Grimaldi, I.; Impemba, S.; Baglioni, P.; Kleij, A. W. Access to Functionalized Polycarbonates Derived from Fatty Acid Esters via Catalytic ROCOP and Their Potential in Gel Formulations. *Macromolecules* **2024**, *57* (8), 3816−3823.
(8) Cui, S.; Borgemenke, J.; Liu, Z.; Keener, H. M.; Li, Y. Innovative Sustainable Conversion from CO2 and Biodiesel-Based Crude Glycerol Waste to Bio-Based Polycarbonates. *J. CO2 Util.* **2019**, *34*, 198−206.
(9) Brandolese, A.; Della Monica, F.; Pericàs, M. À.; Kleij, A. W. Catalytic Ring-Opening Copolymerization of Fatty Acid Epoxides: Access to Functional Biopolyesters. *Macromolecules* **2022**, *55* (7), 2566−2573.
(10) Della Monica, F.; Kleij, A. W. From Terpenes to Sustainable and Functional Polymers. *Polym. Chem.* **2020**, *11*, 5109−5127, DOI: 10.1039/d0py00817f.
(11) Lamparelli, D. H.; Paradiso, V.; Della Monica, F.; Proto, A.; Guerra, S.; Giannini, L.; Capacchione, C. Toward More Sustainable Elastomers: Stereoselective Copolymerization of Linear Terpenes with Butadiene. *Macromolecules* **2020**, *53*, 1665−1673.
(12) Naddeo, M.; Buonerba, A.; Luciano, E.; Grassi, A.; Proto, A.; Capacchione, C. Stereoselective Polymerization of Biosourced Terpenes β-Myrcene and β-Ocimene and Their Copolymerization with Styrene Promoted by Titanium Catalysts. *Polymer* **2017**, *131*, 151−159.
(13) Ricci, G.; Pampaloni, G.; Sommazzi, A.; Masi, F. Dienes Polymerization: Where We Are and What Lies Ahead. *Macromolecules* **2021**, *54* (13), 5879−5914.
(14) Wahlen, C.; Frey, H. Anionic Polymerization of Terpene Monomers: New Options for Bio-Based Thermoplastic Elastomers. *Macromolecules* **2021**, *54* (16), 7323−7336.
(15) Bolton, J. M.; Hillmyer, M. A.; Hoye, T. R. Sustainable Thermoplastic Elastomers from Terpene-Derived Monomers. *ACS Macro Lett.* **2014**, *3* (8), 717−720.
(16) Lamparelli, D. H.; Winnacker, M.; Capacchione, C. Stereoregular Polymerization of Acyclic Terpenes. *ChemPlusChem* **2022**, *87* (1), No. e202100366, DOI: 10.1002/cplu.202100366.
(17) Holzmüller, P.; Gardiner, C.; Preis, J.; Frey, H. CO_2-Based Polycarbonates with Low Glass Transition Temperatures Sourced from Long-Chain Terpenes. *Macromolecules* **2024**, *57*, 5358−5367.
(18) Schüttner, S.; Krappel, M.; Koziol, M.; Marquart, L.; Schneider, I.; Sottmann, T.; Frey, H. Anionic Ring-Opening Copolymerization of Farnesyl Glycidyl Ether: Fast Access to Terpenoid-Derived Amphiphilic Polyether Architectures. *Macromolecules* **2023**, *56*, 6928−6940.
(19) Kobayashi, S.; Lu, C.; Hoye, T. R.; Hillmyer, M. A. Controlled Polymerization of a Cyclic Diene Prepared from the Ring-Closing Metathesis of a Naturally Occurring Monoterpene. *J. Am. Chem. Soc.* **2009**, *131* (23), 7960−7961.
(20) Liu, B.; Li, S.; Wang, M.; Cui, D. Coordination Polymerization of Renewable 3-Methylenecyclopentene with Rare-Earth-Metal Precursors. *Angew. Chem. Int. Ed* **2017**, *56* (16), 4560−4564.
(21) Paradiso, V.; Capaccio, V.; Lamparelli, D. H.; Capacchione, C. [OSSO]-Bisphenolate Metal Complexes: A Powerful and Versatile Tool in Polymerization Catalysis. *Coord. Chem. Rev.* **2021**, *429*, No. 213644.
(22) Capacchione, C.; Saviello, D.; Ricciardi, R.; Proto, A. Living, Isoselective Polymerization of 4-Methyl-1,3-Pentadiene and Styrenic Monomers and Synthesis of Highly Stereoregular Block Copolymers via Sequential Monomer Addition. *Macromolecules* **2011**, *44* (20), 7940−7947.
(23) Proto, A.; Avagliano, A.; Saviello, D.; Ricciardi, R.; Capacchione, C. Living, Isoselective Polymerization of Styrene and Formation of Stereoregular Block Copolymers via Sequential Monomer Addition. *Macromolecules* **2010**, *43* (14), 5919−5921.
(24) Lisovskii, A.; Nelkenbaum, E.; Volkis, V.; Semiat, R.; Eisen, M. S. Polymerization of Isobutylene and Copolymerization of Isobutylene with Isoprene Promoted by Methylalumoxane. *Inorg. Chim. Acta* **2002**, *334*, 243−252.
(25) Zijlstra, H. S.; Harder, S. Methylalumoxane − History, Production, Properties, and Applications. *Eur. J. Inorg. Chem.* **2015**, *2015* (1), 19−43.
(26) Meille, S. V.; Allegra, G.; Geil, P. H.; He, J.; Hess, M.; Jin, J.-I.; Kratochvíl, P.; Mormann, W.; Stepto, R. Definitions of Terms Relating to Crystalline Polymers (IUPAC Recommendations 2011). *Pure Appl. Chem.* **2011**, *83* (10), 1831−1871.
(27) Jeen, H.; Choi, W. S.; Freeland, J. W.; Ohta, H.; Jung, C. U.; Lee, H. N. Topotactic Phase Transformation of the Brownmillerite $SrCoO_{2.5}$ to the Perovskite $SrCoO_{3-\delta}$. *Adv. Mater.* **2013**, *25*, 3651−3656.
(28) Danno, T.; Nakatsuka, D.; Kusano, Y.; Asaoka, H.; Nakanishi, M.; Fujii, T.; Ikeda, Y.; Takada, J. Crystal Structure of β-Fe_2O_3 and Topotactic Phase Transformation to α-Fe_2O_3. *Cryst. Growth Des.* **2013**, *13* (2), 770−774.
(29) Meng, Z.; Yan, H.; Qin, P.; Zhou, X.; Wang, X.; Chen, H.; Liu, L.; Liu, Z. Topotactic Transition: A Promising Opportunity for Creating New Oxides. *Adv. Funct. Mater.* **2023**, *33* (46), No. 2305225.
(30) Garvie, L. A. J.; Nemeth, P.; Buseck, P. R. Transformation of Graphite to Diamond via a Topotactic Mechanism. *Am. Mineral.* **2014**, *99* (2−3), 531−538.
(31) Iuliano, M.; De Rosa, C.; Guerra, G.; Petraccone, V.; Corradini, P. Structural Variations in Ethylene-tetrafluoroethylene Copolymers as a Function of Composition and Temperature. *Makromol. Chem.* **1989**, *190* (4), 827−835.
(32) De Rosa, C.; Auriemma, F. *Crystals and Crystallinity in Polymers: Diffraction Analysis of Ordered and Disordered Crystals*; John Wiley & Sons, 2013; Chap. 4, p 185-295.

https://doi.org/10.1021/acs.macromol.4c01563
Macromolecules 2024, 57, 7409−7417